

Quality Enhancement of Laser Powder-Bed Fusion Parts by Acoustically Assisted Additive Manufacturing by Laser Powder-Bed Fusion and its Application to Lattice Structures

Oliver Maurer* and Dirk Bähre

Additive manufacturing technologies such as laser powder-bed fusion (L-PBF) offer great freedom in design, ultralightweight optimization of components, and individualization of products down to a batch size of one. However, parts fabricated from L-PBF suffer from poor quality. Unavoidable porosity, rough surfaces, anisotropic microstructure, and poor geometrical accuracy and their large scatter pose challenges to post-processing, force larger tolerances, or inhibit technical applications. Acoustic assistance during a build job compacts the powder-bed and has an influence on solidification. This is why the technology addresses all the aforementioned drawbacks. It is known that porosity, surface roughness in downskin regions, and microstructural anisotropy decrease without any post-processing if a build job is sonicated. This study focuses on the fabrication of lattice structures by acoustically assisted L-PBF. Even with a parameter set that is not adjusted to thin-walled structures, porosity decreases in the as-built state. Quasistatic compression tests as well as compressive load increase tests are performed. Results show superior mechanical properties of acoustically assisted samples if compared to standard samples.

1. Introduction and State of Research

Laser powder-bed fusion (L-PBF) is subject to manifold studies. Structures of high geometrical complexities with a high degree of individualized features drive its application in industries, which

rely on customization.^[1] Therefore, L-PBF suits aerospace, racing, and medical applications,^[2] which profit from lightweight and ultralightweight design.^[3] Lattice structures exhibit ultralightweight design potential^[4] and can be used additionally for functional integration of multiphysical effects.^[5,6] Additive manufacturing (AM) provides the only technologies to fabricate such lattice structures with a high degree of geometrical order.^[7] Lattices can be described either by a manageable set of geometrical parameters or using mathematical functions as in the case of triply periodic minimal surface (TPMS) structures.^[8,9]


However, the quality of L-PBFed parts (bulk parts as well as lattices) does not suffice for high-performance applications. Several manufacturing related artifacts in L-PBF reduce the fatigue life, especially if they are close to the surface.^[10] Porosity,^[11,12] rough surfaces,^[13] anisotropic microstructure,^[14] and poor geometrical

accuracy^[15] in the as-built state require post-processing which consumes large amounts of energy as with hot isostatic pressing (HIP) to reduce porosity.^[16] Post-processing technologies from the subtractive sector often require tools to smoothen surfaces, which cannot reach internal structures of lattices.^[17] So, improvements of the as-built state of L-PBF parts are needed to harness the design freedom and possible geometrical complexities while still fulfilling product safety requirements.

Acoustic assistance during L-PBF build jobs is a promising extension for standard L-PBF to achieve higher overall part quality, which was subject to a few studies. Yan et al.^[18] sonicated irradiation phases of build jobs with a cobalt-based super alloy and achieved grain refinement leading to superior mechanical properties in the as-built state. Several research groups applied acoustic assistance to laser metal deposition (LMD) and used ultrasonic waves up to 1000 W in power during LMD.^[19–21] All aforementioned studies on acoustic assistance of AM processes dealt with bulk samples and did not investigate lattice structures. Only Guo et al.^[22,23] produced acoustically assisted bulk parts and gyroid lattice structures, where the sound excitation was applied from the ceiling of the build chamber onto the surface of the powder-bed. They reported grain refinement with their composite material of stainless steel and tungsten

O. Maurer, D. Bähre
Institute of Production Engineering
Saarland University
Campus A4.2, 66123 Saarbrücken, Germany
E-mail: oliver.maurer@uni-saarland.de

O. Maurer, D. Bähre
Department of Manufacturing Technology
Centre for Mechatronics and Automation Technologies (ZeMA)
Eschberger Weg 46, 66121 Saarbrücken, Germany

 The ORCID identification number(s) for the author(s) of this article can be found under <https://doi.org/10.1002/adem.202500318>.

© 2025 The Author(s). Advanced Engineering Materials published by Wiley-VCH GmbH. This is an open access article under the terms of the Creative Commons Attribution License, which permits use, distribution and reproduction in any medium, provided the original work is properly cited.

DOI: 10.1002/adem.202500318

carbide as well as superior mechanical behavior throughout the entire stress–strain–curve of quasistatic compression tests of TPMS lattices.

Fatigue properties of additively manufactured parts are usually analyzed in standardized setups with standardized bulk samples.^[24–26] Usually, the influence of post-processing techniques such as heat treatment, HIP, or machining is investigated.^[24,27] In additively manufactured parts, defects such as porosity, especially if located close to the surface,^[10] tensile residual stress^[28] and surface roughness^[29] induce notches on the micro scale reduce the fatigue life. Depending on the post-processing route, additively manufactured samples can provide more resistance to fatigue damage than wrought parts.^[27] Lattice structures do contain notches not only on the microscale due to surface roughness but also on the macroscale due to its ordered geometry in unit cells. According to Schneller et al.^[24] and Neuber,^[30] the geometrical notch factor K_t depends on the notch depth t and the notch root radius of curvature r as given in Equation (1).

$$K_t = 1 + 2\sqrt{\frac{t}{r}} \quad (1)$$

Van Hooreweder and Kruth^[31] acknowledge the importance of the notch effect by evaluating global and local stress Wöhler curves during fatigue of lattice structures. Global stress evaluation reveals differences due to build orientation of lattices, whereas local analysis does not. Again, heat treatment and HIP enhance fatigue life. Wu et al.^[32] confirmed endured fatigue life for HIPed Ti–6Al–4 V TPMS lattices. Due to notch contributions of the unit cell shape, fatigue life differs significantly as described by Soro et al.^[29] Zargarian et al.^[33] presented Basquin curves for different unit cell types, where, e.g., a Kelvin lattice outperformed a dodecahedron lattice. This seems to have a bigger influence than the stress ratio R , because in a bending-dominated strut-based lattice such as body-centered cubic (BCC), stress states form similarly for several stress ratios due to a redistribution of loads characterized by a Navier symmetrical trend.^[34] Coluccia and De Pasquale^[35] performed alternate bending fatigue tests on strut-based octet truss lattices similar to BCC made of IN625 and sketched a structure specific

and loading specific Haigh diagram which defines a working point beneath a mean stress dependent fatigue limit. Burr et al.^[36] added a chronology of partial failure in strut-based lattices upon applied load cycles. Additionally, Soro et al.^[29] found differences in the failure behavior different lattice types through extensive fractography revealing different types of damages like overstress ductile fractures and fatigue striations on HIPed graded lattices. Collini and Meneghetti^[34] also observed fatigue striations on fracture surfaces whereby failure initiated at surfaces with large amounts of powder particle adhesion from the L-PBF process. Close to the surfaces with particle adhesion, their fractography showed dimples on fracture surfaces. Dimples can form upon fatigue loads and join with pores, a severe issue in AM parts,^[37] to become larger voids and force fracture.^[38]

In conclusion, the current state of research lacks investigations on the producibility and properties of lattice structures produced by acoustically assisted L-PBF. From an application perspective, the question arises, whether superior part quality applies to lattices fabricated from assisted L-PBF and whether these improvements lead to enhanced mechanical properties in quasistatic and cyclic experiments. Literature on fatigue of additively manufactured lattices and bulk samples showed that smoother surfaces and less porosity increase the fatigue life, so acoustic assistance, which achieves both, might increase the fatigue life in the as-built state, either. This study enters these questions by running first build jobs with AlSi10Mg lattices and by evaluating the shape, porosity, and the aforementioned mechanical properties.

2. Experimental Section

2.1. Sample Geometry

The lattice samples were designed in Netfabb Premium 2023 (Autodesk Inc., San Rafael, CA, USA) and consisted of BCC unit cells, as seen in **Figure 1a**, with a strut diameter of 0.75 mm in an arrangement of $3 \times 3 \times 3$ unit cells in x, y, and z direction as suggested by Kollmannsperger et al.^[39] and BCC lattices are a widely used kind of strut-based lattices and do not provide any multiphysical effects like oscillation damping or the auxetic effect.^[8,9,40] In this study, a single unit cell measured 2.5 mm,

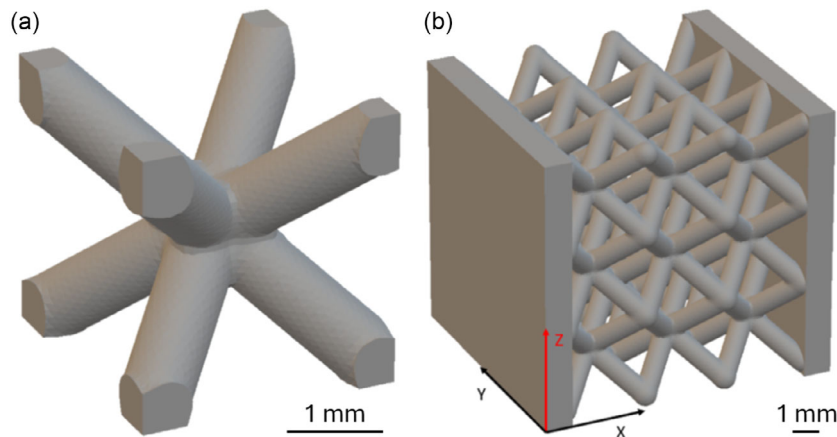


Figure 1. Sample geometry of this study: a) single BCC unit cell and b) complete $3 \times 3 \times 3$ arrangement including cover plates.

so the strut length per unit cell was 2.9 mm. One entire lattice sample measured $11 \times 10 \times 10$ mm. This anisotropy arose from the usage of 1 mm thick cover plates at both ends in x direction, which overlapped the outer struts ends by 0.5 mm. These plates shall assure proper contact with testing machines and, by that, lead to smooth loading of the lattice cells. However, during a build job, more heat must be conducted out of plates than out of the lattice. Therefore, the samples were built along z direction and tested along x direction, as defined in Figure 1b.

2.2. L-PBF

An SLM125 (Nikon SLM Solutions AG, Lübeck, Germany) with a cube-shaped build volume of $125 \times 125 \times 125$ mm fabricated all standard L-PBF samples of this study. AlSi10Mg powder (Nikon SLM Solutions AG, Lübeck, Germany) with a particle size distribution between 20 and $63 \mu\text{m}$ served as a feedstock material. Its relative moisture content was kept $<10\%$ to ensure proper layer spreading ability. The composition as declared by the manufacturer's material data sheet^[41] is given in Table 1. Argon served as a shielding gas to avoid oxidation during the run of every build job.

Standard-L-PBF and acoustically assisted L-PBF lattices were produced with different parameter sets. As described by Kollmannsperger et al.^[39] a suitable parameter set to manufacture AlSi10Mg lattices with this type of L-PBF machine is the one given in Table 2. Total fill as a scan strategy means that in each layer the laser starts with the contour and continues to scan nested lines similar to the contour until the whole area is scanned according to the current slice.

Magics software (Materialise NV, Leuven, Belgium) was used to define sample positions on the substrate, to place support structures, to assign parameter sets and to create a sliced.slm file. Support structures separated the samples from the substrate to remove the samples by sawing. Lattice structures support themselves, so no additional support structures were required on their inside. As depicted in Figure 1, samples have cover plates attached to the lattice. The plates had line supports, whereas

lattice nodes facing downward had pole supports to conduct process heat from the laser incidence toward the substrate.

2.3. Acoustically Assisted L-PBF Part Fabrication

Acoustically assisted L-PBF was performed by the same SLM125 L-PBF machine, that produced all standard L-PBF samples. The extension kit for acoustic assistance had a smaller, cylindrically shaped build volume (diameter 60 mm, height 36 mm) and excited the substrate from below with white noise sonication at 3.5 W acoustic power amplitude for AlSi10Mg. White noise excited the powder-bed with numerous frequencies simultaneously using several frequencies that compact the powder-bed at once. It could be described by a linear increase of sound intensity I over the frequency f , so $\frac{dI}{df} = \text{const.}$ applied with a difference of 3 dB for successive octave bands.^[42,43] The acoustic power of 3.5 W marked the maximum in this setup at which the transducer Eliga 85 977 (Elsässer GmbH, Augsburg, Germany) connected to the amplifier The t.amp E400 (Thomann GmbH, Burgebrach, Germany) endured an entire build job. Due to the installation of the extension kit on the inside of the machine, the substrate could not be heated anymore during build jobs. To date no parameter set has been adjusted to both lattice structures and acoustic assistance. The parameter set used to fabricate the assisted lattices, as seen in Table 3, is the currently known optimum of this hybrid manufacturing technology of AlSi10Mg bulk parts. Hatch as scan strategy meant that a chessboard-like line pattern in the center of an irradiated area got scanned first, followed by the contour of this specific area. The maximum scan vector length amounted 15 mm.

2.4. Sample Characterization

After fabrication, samples were cut off the substrate with an automatic saw. Then, support structures were manually removed from the samples. Despite that, no post-processing occurred, so all samples remained in their as-built state for better comparability of standard and acoustically assisted L-PBF.

Table 1. Chemical composition of the AlSi10Mg feedstock powder used in this study.^[41]

Element	Al	Si	Mg	Fe	Mn	Ti	Zn	Cu	Ni	Pb	Sn	Other total
Mass fraction [wt%]	Balance	9–11	0.45	0.55	0.45	0.15	0.10	0.05	0.05	0.05	0.05	0.15

Table 2. Parameter set that fabricated AlSi10Mg lattice structures in the standard L-PBF mode.^[39]

Parameter	Powder layer thickness [μm]	Laser power [W]	Scan speed [mm s^{-1}]	Hatch distance [mm]	Substrate heating [K]	Scan strategy
Value	30	250	2000	0.1	423	Total fill

Table 3. Parameter set that fabricated AlSi10Mg lattice structures in the acoustically assisted L-PBF mode.

Parameter	Powder layer thickness [μm]	Laser power [W]	Scan speed [mm s^{-1}]	Hatch distance [mm]	Substrate heating [K]	Scan strategy
Value	30	250	1650	0.06	none	Hatch

2.4.1. Density Measurement

Relative density means in this study the counterpart to porosity inside the material and must not be confused with relative density as it is often used in the cellular materials community meaning the degree to which the volume of a bounding box is filled with material. This counterpart to porosity was measured in an Archimedean measurement setup mounted on a precision balance AT200 (Mettler Toledo, Columbus, OH, USA, accuracy ± 0.15 mg). Weighing of all samples took place three times in ambient air and three times in water immersion. However, the water container made no contribution to weighing results. Before weighing samples in water immersion, they were dipped into ethanol to enhance wetting of the water and, by that, to avoid air bubbles pinning on lattice surfaces. This AlSi10Mg alloy had a theoretical mass density of $\rho_{th} = 2.67 \frac{g}{cm^3}$.^[41] With respect to the mean sample masses weighed in air \bar{m}_a and water \bar{m}_w as well as the density of the immersion water $\rho_w(T)$, which was read off a table depending on the temperature T , the relative density ρ_r was defined by Equation (2).^[44] Twenty samples per L-PBF mode were analyzed.

$$\rho_r = \frac{1}{\rho_{th}} \frac{\bar{m}_a \rho_w(T)}{\bar{m}_a - \bar{m}_w} \quad (2)$$

2.4.2. Cross-Section Calculations

Stress tended to concentrate at small cross sections and sharp radii.^[30,38] Both were present in lattice structures and the cross sections varied greatly. Consequently, an evaluation of cross-section area depending on the position of the sample along the direction of loading helped to understand responses to external loads. The analysis of this sample geometry was based on the designed file neglecting shape deviations in real parts and used a custom-made Python code.

The examination of the geometry was conducted according to limit values in all three Cartesian directions (x_{min} , x_{max} , y_{min} , y_{max} , z_{min} , z_{max}). A reference volume was then created in which the volume of the STL geometry could be examined. After conversion into a LabelMap, it divided the volume or mesh into individual, discrete voxels (3D pixels). The volume was therefore cut in defined integer steps with respect to the x , y , and z axes, with the voxels assuming a discrete value. The LabelMap was converted into a NumPy array and iterated over 1D to obtain the pixels of a plane (cross section). Each cross-section plane was saved using ImageIO, a Python library that can create image files. After the generation of a stack of images, the surface calculation was performed by threshold segmentation. This was followed by the calculation of the areas with the 3D Slicer freeware. It was important to note that the result must be divided by two, as the 3D segmentation in 3D Slicer creates a front and a back-side of the 2D image. This was done image by image and the area calculation was carried out by 3D Slicer's Segmentation Statistics library. The result of the surface calculation was also added or saved in a .txt file after each layer and could be plotted afterward.

2.4.3. Microstructural Analysis

During metallographic preparation of one sample per L-PBF mode, filigree struts and nodes of the lattices shall not be damaged.

Therefore, one standard L-PBF and one assisted L-PBF sample were put in cylindrical molds and infused with Demotec 30 (Demotec Demel, Nidderau, Germany) resin. This type of resin dissolves in acetone. Grinding on SiC sandpapers (graining 320, 600, 800, 1200) and polishing on textile cloths (6 and 3 μ m diamond suspension as well as oxide polishing suspension, silica OPS) lead to low-in scratch surfaces. The quality of the preparation was checked using the digital microscope VHx7000 (Keyence Corp., Osaka, Japan). Afterward, the resin was dissolved in acetone immersion for 24 h.

A scanning electron microscope (SEM) Sigma VP (Carl Zeiss AG, Oberkochen, Germany) equipped with an electron backscatter diffraction (EBSD) detector Nordlys (Oxford Instruments PLC, Abingdon, UK) recorded patterns with a step size of 1 μ m. Afterward, HKL Tango software and ATEX software^[45] processed data to calculate grain diameters, to create orientation maps and to plot pole figures.

2.4.4. Compression Tests

Quasistatic compression tests at room temperature and a displacement rate of 0.16 mm s^{-1} , which equaled a strain rate of 0.015 s^{-1} , were performed using a Doli 851 120 (Instron GmbH, Darmstadt, Germany) to determine plastic collapse loads and corresponding deformations. Tests ended at a maximum displacement of 6 mm or when the crossbeam force dropped by at least 50%. Five samples of each L-PBF mode were tested to assure statistical confidence of the results.

2.4.5. Load Increase Fatigue Tests

Cyclic tests were performed using a three-mass resonance pulser Rumul Mikrottron (Russenberger Prüfmaschinen AG, Switzerland). Two plates fixed the sample in-between during the entire test to prevent slipping. To induce testing loads into the sample as even as possible, the upper fixture plate was connected with the machine via a double knee joint. All tests ran with constant stress ratio of $R = 2$ in compression and reached a resonant testing frequency of about 200 Hz. The discrete load stages were defined with respect to the plastic collapse forces (PCF) as results of the quasistatic experiments, as depicted in **Figure 2**. If the fatigue life of samples exceeded the fifth stage,

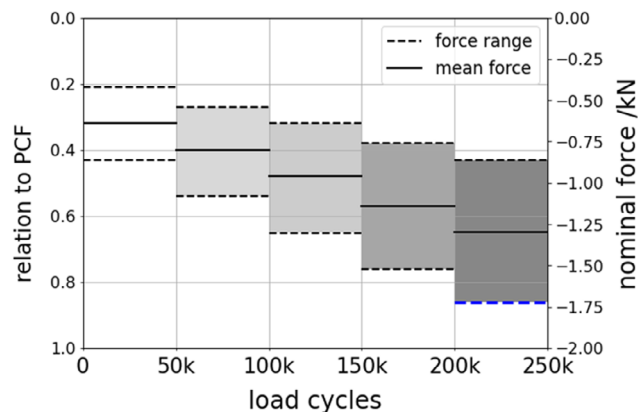


Figure 2. Force stages of the load increase tests in absolute measures and their relation to the mean plastic collapse force (PCF).

tests went on to a sixth stage increasing mean force and force range by the same amount as in precedent stages while keeping $R = 2$. The failure criterion was either sample disintegration or a change in resonance frequency by 10 Hz. Forces were measured throughout all tests with a 20 kN load cell. For each L-PBF mode, 15 samples were tested.

3. Results and Discussion

3.1. Manufacturability and Relative Density

Acoustically assisted lattices are as manufacturable as their standard L-PBF counterparts. The support strategy chosen for standard L-PBF worked for assisted L-PBF, either. At the stage of removing samples from their substrate, cover plates tend to fall off the lattices after assisted L-PBF. This points toward bonding issues between these two sample sections. During the check of metallographic preparation, digital microscopy revealed that large pores at the transition from cover plate to strut existed and probably lead to this observation, as seen in Figure 3. Probably, struts, which have free ends before they are bonded with other struts or cover plates to form closed contours during the build job, oscillate differently upon sonication with white noise than the cover plate. The usage of multiple frequencies may induce different resonant frequencies and, by that, different oscillation modes into the process. This might cause larger gaps that remain unfilled and single-frequency sonication might lead to better bonding.

Archimedean density measurements must clarify whether these bonding issues increase porosity. The overall impression of Figure 3a,b does not seem that acoustic assistance reduces porosity at all, but this probably comes from the comparison of two single images representing two single 2D cross-sections. Table 4 summarizes mean values and standard deviations of the density measurement results of 20 samples per L-PBF mode. It becomes obvious that the relative density of lattices from assisted L-PBF exceeds the one of lattices from standard L-PBF by 1.2 percentage points, so acoustic assistance decreases porosity. Archimedean density measurements oppose the impression of the micrographs in Figure 3, but Archimedean density gives data from an entire sample while one single metallographic cross section does not contain volumetric information. Consequently, the data shown in Table 4 is more reliable than the micrographs in Figure 3. However, relative density values are below expectations of bulk materials, which usually exceed 99%.^[44] Insufficient wetting of the water immersion especially on rough downskin

Table 4. Results of the Archimedean density measurements of standard and assisted L-PBF lattices.

L-PBF mode	Standard	Acoustically assisted (white noise @ 3.5 W)
Mean relative density [%]	97.2	98.4
Standard deviation [%]	0.5	0.8

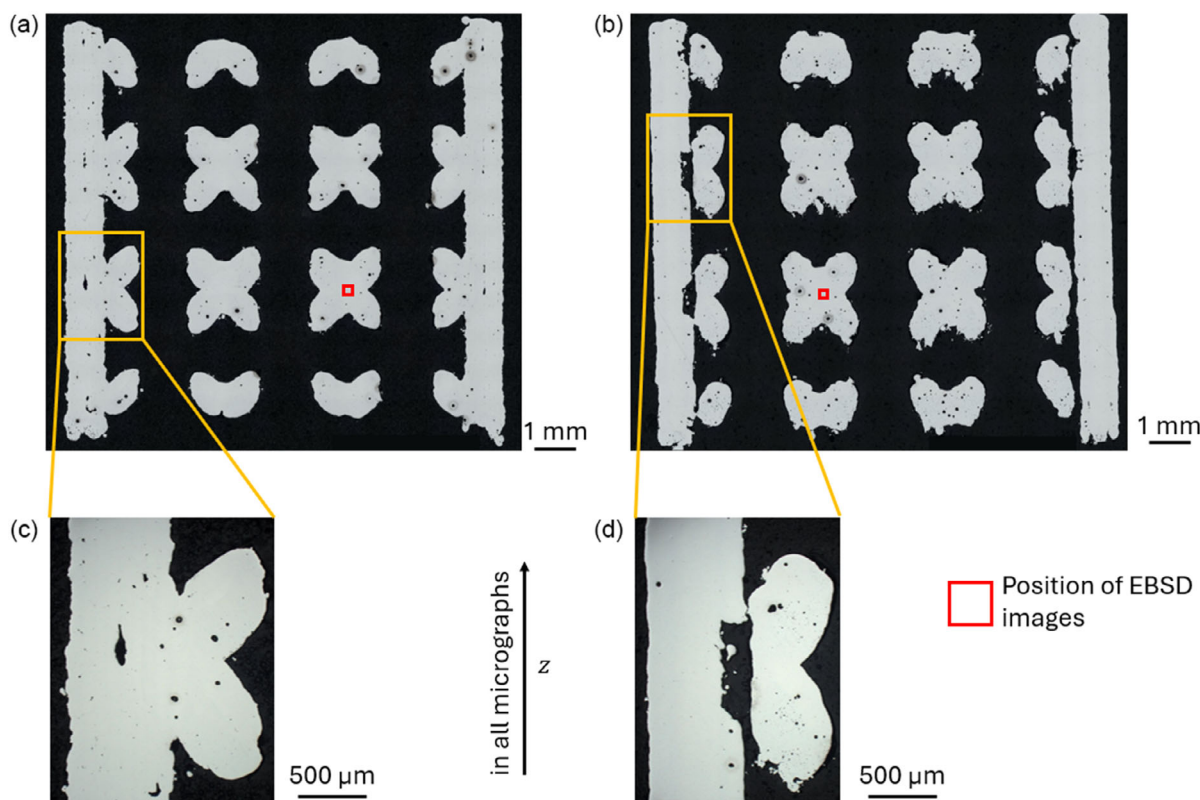


Figure 3. Digital microscopy images of a,c) a standard L-PBF lattice and b,d) an acoustically assisted L-PBF lattice; build direction goes from bottom to top in all micrographs.

surfaces can lead to small residual air bubbles remaining on these surfaces. This results in lower weights of samples in water immersion and, by that, in lower density values. Dipping all the samples in ethanol before weighing in water immersion reduces this effect but apparently did not eliminate it. However, measurement results are comparable to each other because all samples were treated in the same way.

3.2. Microstructural Analysis

All lattices are expected to fail at nodes during fatigue testing due to stress concentration in notch roots on six sides of each node. Therefore, the microstructure inside nodes is defined as the region of interest. EBSD images of a squared size with an edge length 200 μm in **Figure 4** reveal the grain structure as well as the grain orientation. Both images show columnar crystals, which are part of a superordinate fish scale-like structure as described in literature.^[46–48] However, EBSD images of **Figure 4** differ with respect to present colors representing grain orientation. Assisted L-PBF obviously leads to more diverse grain orientations represented by more diverse colors in **Figure 4b** than in **Figure 4a**. White noise excitation results in an omnipresent oscillation, so solidification occurs in the presence of numerous frequencies. These frequencies excite nuclei when they form and tend to rotate them slightly depending on the volatile noise amplitude. Consequently, more random orientations occur.

Additionally, it seems that acoustic assistance can lead to grain refinement, even if it does not eliminate columnar crystal growth. The equivalent grain diameter d_{eq} , as given in **Table 5**, describes the diameter, an exactly spherical grain would have if it had the same area as measured. The formula to calculate equivalent grain diameters is given in Equation (3) using A as the mean pore area extracted from the EBSD images.

$$d_{\text{eq}} = \sqrt{\frac{4A}{\pi}} \quad (3)$$

Acoustic assistance with white noise at 3.5 W leads to grain refinement as equivalent diameters in **Table 5** show. Obviously,

Table 5. Results of the EBSD measurements of standard and assisted L-PBF lattices.

L-PBF mode	Standard	Acoustically assisted (white noise @ 3.5 W)
EBSD index rate [%]	81	85
Mean equivalent grain diameter [μm]	13.84	9.81
Mean grain aspect ratio [–]	0.43	0.46

the effect is not as strong as in ultrasonic assisted LMD at 125–1000 W^[20,21] due to tremendously lower acoustic power levels in this study and the absence of cavitation. Nevertheless, sound seems to contribute to the energy considerations of nucleation leading to an increased nucleation rate. Beyond the mean values of **Table 5**, cumulative frequency plots of **Figure 5** allow for an insight into statistics. **Figure 5a** shows that more grains in the assisted L-PBF lattice node have small areas because its curve starts higher than its standard counterpart and reaches the maximum relative cumulative frequency of 1 at smaller grain areas. So, the grain refining effect of acoustic assistance becomes evident.

Figure 5c gives distributions of the equivalent grain diameters to assure statistic confidence of the presented results. Obviously, more grains in the assisted L-PBF lattice have smaller equivalent diameters than in the standard L-PBF lattice. Due to grain refinement, the total number of grains in the EBSD image of assisted L-PBF exceeds the number of grains of standard L-PBF. In the case of standard L-PBF, the first and third bins of the histogram are equally high. In the case of assisted L-PBF, the first bin is much larger than the third or any other subsequent bin which proves grain refinement again.

Aspect ratios describe the quotient of the minimum diameter of one grain divided by its maximum diameter. Spherical grains would have an aspect ratio of 1, more randomly shaped or columnar grains are between 0 and 1. As seen in **Table 5** and **Figure 5b**, aspect ratios of standard and assisted L-PBF lattice nodes do not differ greatly. It seems that even if acoustic assistance refines grains the microstructure has almost the same preferential

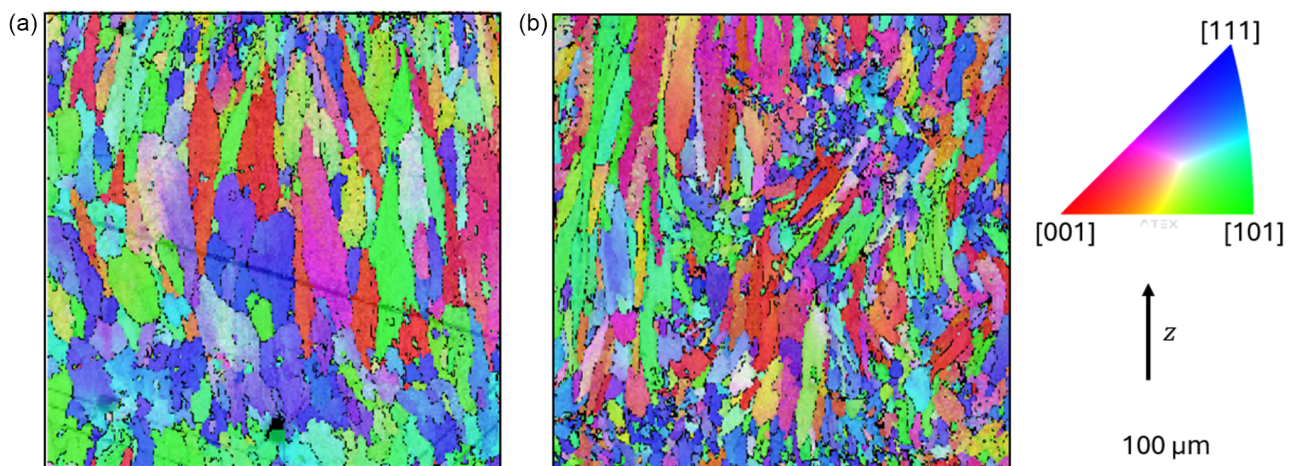


Figure 4. EBSD images of a) a standard L-PBF lattice node with 381 grains and b) an acoustically assisted L-PBF lattice node with 1304 grains; build direction goes from bottom to top in all images.

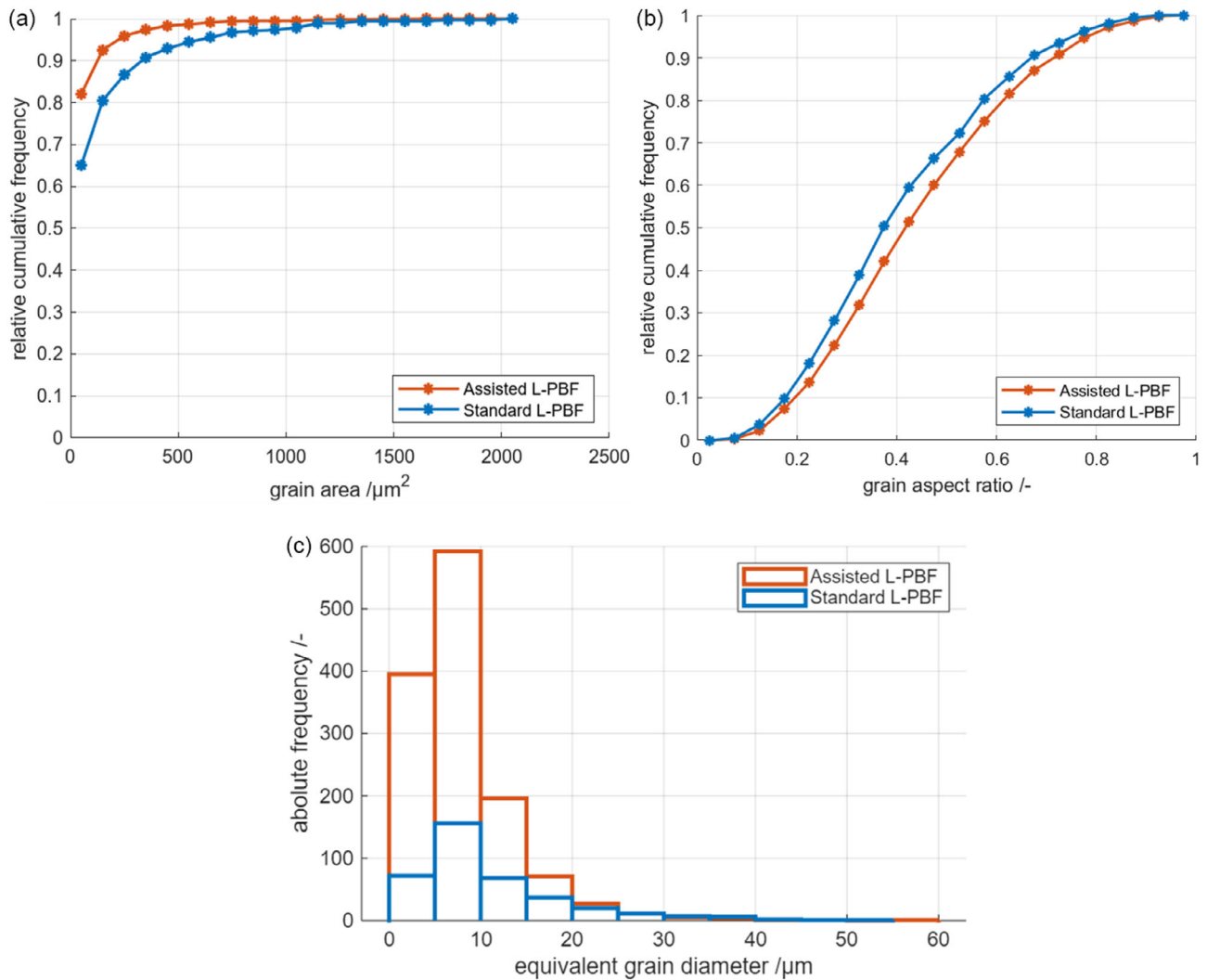


Figure 5. Cumulative frequency plots of a) grain area distributions, b) grain aspect ratio distributions, and c) equivalent grain diameter histograms of both, standard and acoustically assisted L-PBF.

orientation as with standard L-PBF. Figure 5b reveals slight differences between both L-PBF modes. The relative cumulative frequency curve of the assisted L-PBF runs below the curve of standard L-PBF. This means that fewer grains with low aspect ratios form upon sonication, so there is a slight tendency to form rather equiaxed grains. However, columnar crystal growth is still present.

Pole figure calculation in ATEX software based on the EBSD data shall clarify the degree to which preferential orientations exist in both microstructures. As seen in **Figure 6**, cross-shaped patterns form in both pole figures implying similar preferential orientations. These originate from the strong thermal gradient through the already built part from the laser incidence down to the substrate. Despite their general shape, pole figures of standard and assisted L-PBF lattice nodes deviate regarding intensity of patterns. Figure 6a corresponding to standard L-PBF has more intense hotspots, whereas Figure 6b corresponding to acoustically assisted L-PBF shows a more diffuse pattern. Hence,

acoustic assistance reduces preferential orientation in the microstructure and it is expected that this effect will increase upon higher acoustic power.

3.3. Cross-Section Calculation

Nominal stress definitions based on external forces divided by the minimum cross-section area, which is hard to measure on 3D lattice structures. To determine the strength of lattices and to compare them to data from the material data sheet, the cross-section area is calculated from the computer aided design (CAD) file using 3D Slicer freeware and a Python script.

The curve of **Figure 7** depicts the cross-section area evolution depending on the x coordinate and the minimum cross-section area of the samples amounts 9.69 mm^2 . Between $x = 0.5 \text{ mm}$ and $x = 1.0 \text{ mm}$ as well as between $x = 10.0 \text{ mm}$ and $x = 10.5 \text{ mm}$, the curve contains artifacts of the segmentation, because the sample geometry consists of three joined STL parts,

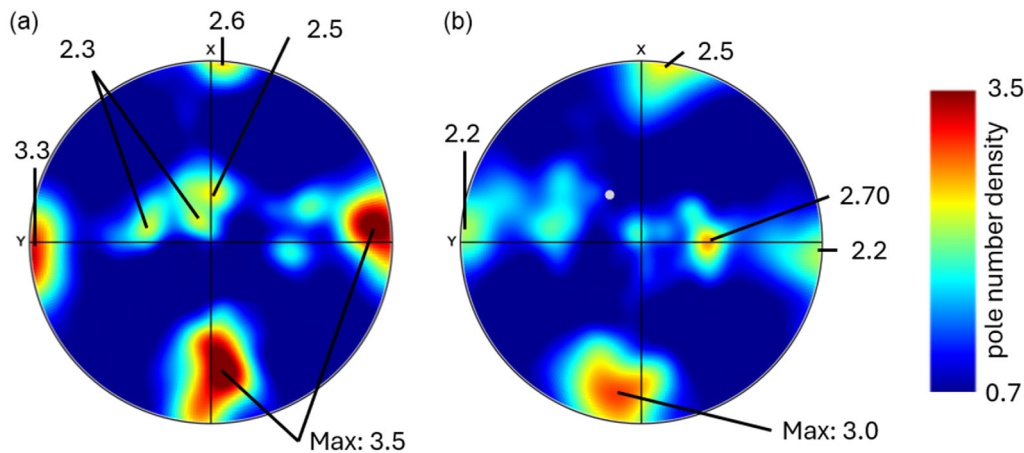


Figure 6. (100) pole figures from EBSD data of a) a standard L-PBF lattice node and b) an acoustically assisted L-PBF lattice node; the points of highest pole number density were quantified.

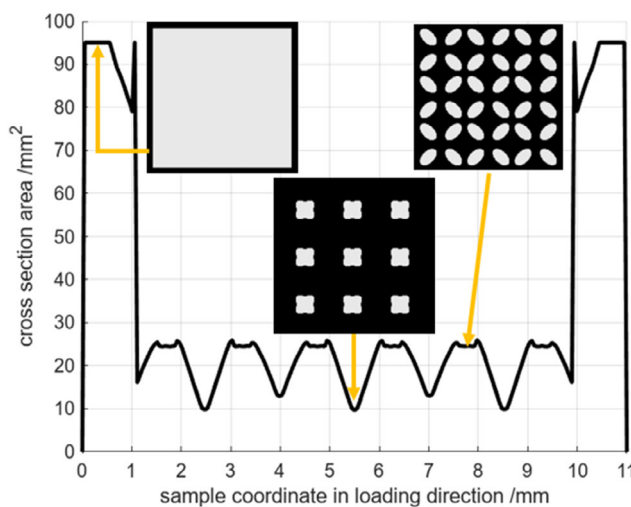


Figure 7. Cross-section area of the lattice samples along the loading direction (x direction in Figure 1) of quasistatic and cyclic tests.

two cover plates and one lattice. In the area of their overlap in the CAD file, these artifacts occur but do not affect physical samples. The oscillating part of the curve corresponds to the BCC lattice. Local minima alternate between two cross-section areas. This is due to the difference in node numbers, which is 9 when nodes connect struts pointing toward the sample center and 16 when nodes connect struts pointing out of the sample. Plateaus in between the minima arise from struts, which are inclined to the x direction. Their projections become visible in the segmented sections.

3.4. Compression Testing

Quasistatic compression tests are at first presented as force–displacement curves to determine the PCF, which is afterward converted into a plastic collapse stress (PCS) as a measure of strength. **Figure 8** summarizes five tests per L-PBF mode

and **Table 6** gives data of the plastic collapse, which marks the first local maximum of curves due to the failure of the first layer of lattice unit cells. Each additional elevation in the curve represents the failure of another layer of lattice unit cells. Two load–displacement curves of standard L-PBF lattices deviate from the others, whereas curves of acoustically assisted lattices scatter less. Standard L-PBF lattices were produced on larger substrate than their assisted counterparts, where effects of part position can alter cooling and pore formation conditions. These effects became obvious in the study of Kollmannsperger et al.^[39] However, the test results show the same PCF for both L-PBF modes and curves tend to superpose each other. Only the displacement at plastic collapse is higher for acoustically assisted L-PBF samples. The strain at plastic collapse, calculated as displacement divided by initial height, confirms this observation and amplifies the difference in deformation. So, acoustic assistance leads to more ductile lattice samples.

PCS values are calculated with the quotient of PCF divided by the minimum cross-section area, which was discussed before. This calculation neglects the location of failure. It is expectable that nodes are the origin of failure due to stress concentration because of the notch effect. However, standard and assisted L-PBF lattice samples do not differ from each other. Their PCS of 194 MPa is similar to the tensile yield strength of 224 MPa found by Sert et al.^[49] on bulk samples, which were loaded perpendicular to the build direction. On the assumption that the material behaves identical upon tension and compression, the PCS is plausible. The decrease of 30 MPa compared to the literature is probably due to bending-dominated deformation of inclined struts in the BCC lattice structure.

3.5. Load Increase Fatigue Testing

Load increase fatigue tests assure that samples fail during the test. Since all samples of both L-PBF modes remained in their as-built state, all samples broke brittle in the x – z plane (as defined by Figure 1) along a diagonal line parallel to the struts. A χ^2 test for the measured fatigue life confirmed a normal distribution for

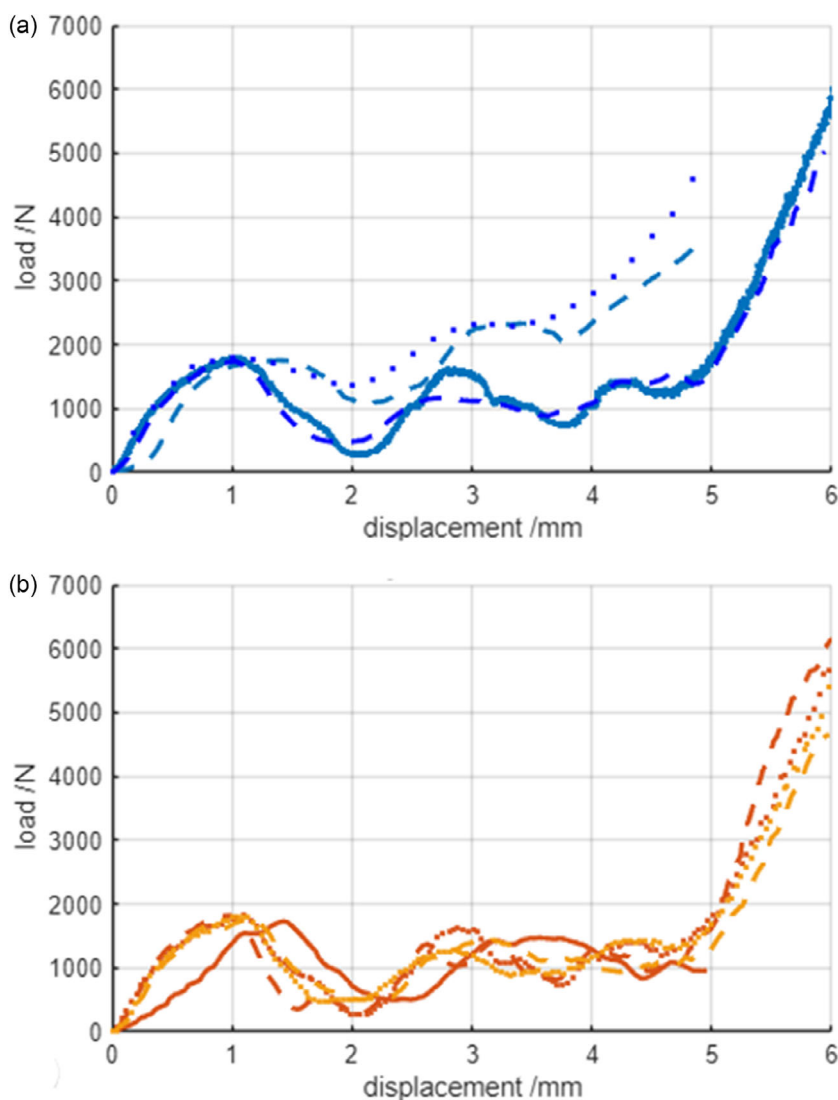


Figure 8. Force–displacement curves of lattice samples loaded along x-direction (see Figure 1) of a) standard and b) acoustically assisted L-PBF.

Table 6. Results of the quasistatic compression tests of standard and assisted L-PBF lattices.

L-PBF mode	Standard	Acoustically assisted (white noise @ 3.5 W)
Plastic collapse force [N]	1881 ± 34	1883 ± 38
Plastic collapse stress [MPa]	194 ± 4	194 ± 4
Displacement at plastic collapse [mm]	1.02 ± 0.14	1.11 ± 0.17
Strain at plastic collapse [%]	9.27 ± 0.01	10.09 ± 0.02

both L-PBF modes at 99% confidence. The number of load cycles to failure N_f and the scatter involved is illustrated in **Figure 9**. Box plots contain the median value (red line), 1.35 times the standard deviation (blue box), 5.4 times the standard deviation (dashed black error bar), and outliers (red crosses).^[50] Arithmetic mean values of N_f differ by $\approx 40\,000$ load cycles.

This is probably due to the bonding issues between cover plates and lattice, which alter the way how load is induced in the lattice region and which provide additional notches. Despite that, the scatter (single standard deviation) of N_f decreases by almost one order of magnitude with assisted L-PBF if compared to the standard.

Several measurands are recorded during the load increase tests. The mean compressive displacement, see **Figure 10a**, displays discrete load levels. Again, lattices from acoustically assisted L-PBF deform stronger due to increased ductility. This increased ductility becomes more obvious at the end of the test before the sample fails. Within the last load stage before failure, all samples deform more than within the previous ones. This final deformation Δu amounts $\Delta u_A \approx 0.065$ mm for assisted L-PBF lattices, which exceeds the final deformation of the standard counterpart $\Delta u_S \approx 0.028$ mm by a factor of 2.3.

Both curves of assisted L-PBF lattices in **Figure 10** contain artifacts and dip at the beginning of the measurement. This is

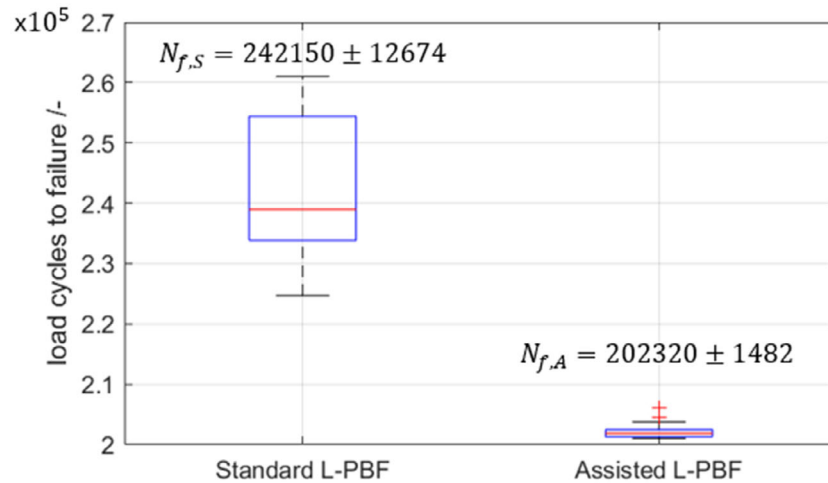


Figure 9. Box plots of load cycles to failure measured on each 15 samples in the load increase test of this study.

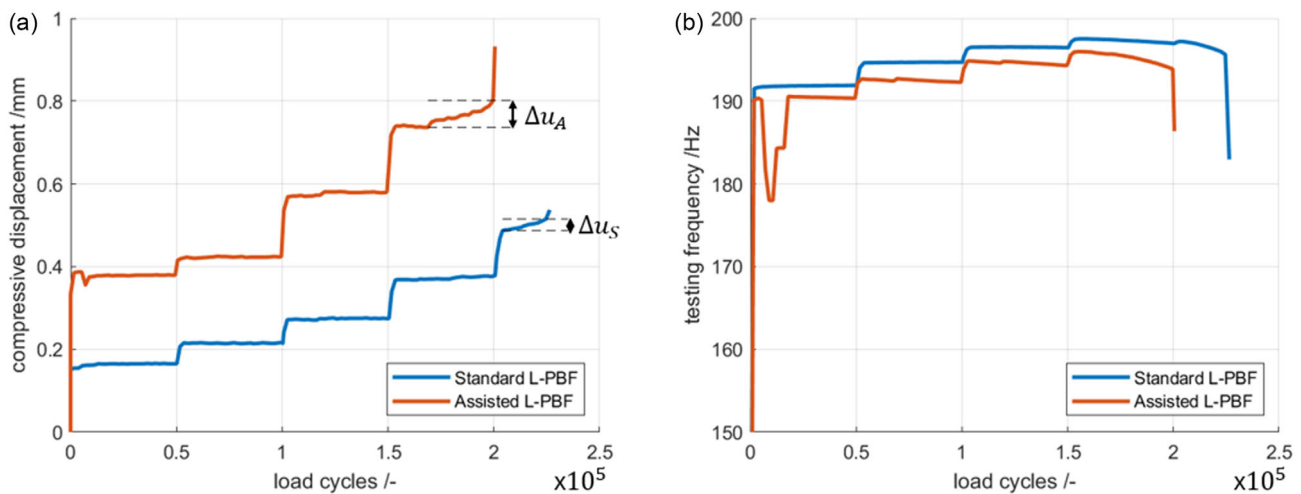


Figure 10. Evolution of a) mean compressive displacement and b) testing resonant frequency during load increase tests of standard and assisted L-PBF lattices, mean curve of 15 samples per L-PBF mode.

probably due to longer transient oscillations and first reactions of the defective bonding between cover plates and lattice. Afterward, the testing frequency is stable as seen in Figure 10b. Load increase tests of assisted L-PBF lattices run at slightly lower frequencies than their standard counterparts, which indicates lower stiffness in this resonant testing setup.^[39] This matches the enhanced ductility in quasistatic and cyclic loading.

4. Conclusion and Future Research

In this study, manufacturability and properties of lattice structures fabricated from acoustically assisted L-PBF with white noise at 3.5 W were investigated. Microstructural effects and higher ductility of acoustically assisted samples were observed. The main findings are 1) acoustically assisted L-PBF can produce lattice structures. Even if there are defective bonds between cover plates and the lattice, the assistance results in rather superior part

quality. 2) Lattices fabricated from assisted L-PBF outperform the relative density of their standard counterpart by 1.2 percentage points in spite of pore formation at the transition from cover plate to lattice. 3) Acoustic assistance refines grains in lattice nodes and expectably in the whole lattice structure but has only a small effect on producing more equiaxed grains. However, preferential orientations inside the microstructure decrease with acoustic assistance. 4) PCF or stress does not differ, but acoustically assisted lattices performed more ductile than their standard counterparts. 5) With respect to the minimum cross-section area of these lattices, strength values were compared to literature and used to validate the experiments. 6) In the same load increase test, the samples of assisted L-PBF last shorter, but the scatter of their load cycles to failure undercuts the scatter of standard L-PBF lattices by one order of magnitude. 7) Load increase tests confirmed the higher ductility of assisted L-PBF lattices by higher mean displacements during the whole test and larger deformation right before failure.

Future research should focus on more stable bonds between lattices and cover plates, e.g., by testing single-frequency sonication. If more acoustic power increases the observed effect on the microstructure and leads to rather small equiaxed grains, lattices in the as-built state could be strengthened and could last longer under fatigue loads. To generalize these findings, experiments with other lattice structures and with other unit cell sizes, types or arrangements need to be performed. Especially the difference between strut-based (like BCC structures) and wall-based (like TPMS structures) lattices might be of special interest. Additionally, fatigue tests with single force or stress amplitudes to gain Wöhler curves of these structures would provide insights into their endurance. These tests would give reliable fatigue life data and would focus on more application-oriented loading frequencies for both modes. Damaging states on microlevel and macrolevel could then further support the findings of this study.

Acknowledgements

The authors thank Prof. Dr. Christian Motz (the chair of the Department of Material Science and Technology) for the opportunity to use the fatigue testing and SEM facilities and the Fraunhofer Institute for Nondestructive Testing (IZFP) to assist with the load increase tests. The authors thank the European Regional Development Fund (ERDF) for supporting their research within the project "iSMAT." The L-PBF machine used to produce the samples in this contribution was generously funded by Deutsche Forschungsgemeinschaft (DFG) in the State Major Instrumentation program with the reference INST 256/503-1 FUGG.

Open Access funding enabled and organized by Projekt DEAL.

Conflict of Interest

The authors declare no conflict of interest.

Author Contributions

Oliver Maurer: conceptualization (lead); data curation (lead); investigation (lead); methodology (lead); resources (lead); software (lead); visualization (lead); and writing—original draft (lead). **Dirk Bähre:** formal analysis (lead); funding acquisition (lead); project administration (lead); supervision (lead); validation (lead); and writing—review and editing (lead).

Data Availability Statement

The data that support the findings of this study are available from the corresponding author upon reasonable request.

Keywords

acoustic assistances, additive manufacturings, fatigues, lattice structures, laser powder-bed fusions (L-PBFs)

Received: January 31, 2025

Revised: May 7, 2025

Published online: June 11, 2025

- [1] I. Gibson, D. Rosen, B. Stucker, M. Khorasani, *Additive Manufacturing Technologies*, Springer International Publishing, Cham **2021**.

- [2] *A Guide To Additive Manufacturing* (Eds: D. Godec, J. Gonzalez-Gutierrez, A. Nordin, E. Pei, J. Ureña Alcázar), Springer International Publishing, Cham **2022**.
- [3] G. Li, C. Zhao, Y. Huang, Q. Tan, J. Hou, X. He, C. Guo, W. Lu, L. Zhou, S. Liu, L. Zhang, X. Chen, X. Li, Y. Li, J. Luan, Z. Li, X. Mao, M.-X. Zhang, Q. Zhu, J. Lu, *Mater. Today* **2024**, 76, 40.
- [4] A. Großmann, J. Gosmann, C. Mittelstedt, *Mater. Sci. Eng. A* **2019**, 766, 138356.
- [5] S. Bronder, F. Herter, A. Röhrig, D. Bähre, A. Jung, *Adv. Eng. Mater.* **2022**, 24, 2100816.
- [6] M. Yang, P. Sheng, *Annu. Rev. Mater. Res.* **2017**, 47, 83.
- [7] M. Benedetti, A. Du Plessis, R. O. Ritchie, M. Dallago, N. Razavi, F. Berto, *Mater. Sci. Eng. R Rep.* **2021**, 144, 100606.
- [8] N. Khan, A. Riccio, *Prog. Aerosp. Sci.* **2024**, 149, 101021.
- [9] M. Helou, S. Kara, *Int. J. Comput. Integr. Manuf.* **2018**, 31, 243.
- [10] S. Romano, A. Brückner-Foit, A. Brandão, J. Gumpinger, T. Ghidini, S. Beretta, *Eng. Fract. Mech.* **2018**, 187, 165.
- [11] H. Hyer, L. Zhou, S. Park, G. Gottsfriz, G. Benson, B. Tolentino, B. McWilliams, K. Cho, Y. Sohn, *Metallogr. Microstruct. Anal.* **2020**, 9, 484.
- [12] P. Ferro, R. Meneghello, S. M. J. Razavi, F. Berto, G. Savio, *Phys. Mesomech.* **2020**, 23, 256.
- [13] O. Maurer, F. Herter, D. Bähre, *J. Manuf. Process.* **2022**, 80, 659.
- [14] N. O. Larrosa, W. Wang, N. Read, M. H. Loretto, C. Evans, J. Carr, U. Tradowski, M. M. Attallah, P. J. Withers, *Theor. Appl. Fract. Mech.* **2018**, 98, 123.
- [15] J. P. M. Pragana, R. F. V. Sampaio, I. M. F. Bragança, C. M. A. Silva, P. A. F. Martins, *Adv. Ind. Manuf. Eng.* **2021**, 2, 100032.
- [16] D. Herzog, K. Bartsch, B. Bossen, *Addit. Manuf.* **2020**, 36, 101494.
- [17] E. Maleki, S. Bagherifard, M. Bandini, M. Guagliano, *Addit. Manuf.* **2021**, 37, 101619.
- [18] Z. Yan, V. Trofimov, C. Song, C. Han, Y. Yang, C. Yang, Y. Xiao, Z. Deng, J. Chen, *J. Alloys Compd.* **2023**, 939, 168771.
- [19] C. J. Todaro, M. A. Easton, D. Qiu, D. Zhang, M. J. Bermingham, E. W. Lui, M. Brandt, D. H. StJohn, M. Qian, *Nat. Commun.* **2020**, 11, 142.
- [20] C. J. Todaro, M. A. Easton, D. Qiu, M. Brandt, D. H. StJohn, M. Qian, *Addit. Manuf.* **2021**, 37, 101632.
- [21] Y. Zhang, Y. Guo, Y. Chen, L. Kang, Y. Cao, H. Qi, S. Yang, *Metals* **2019**, 9, 1111.
- [22] A. Guo, R. Tang, S. Guo, Y. Hu, X. Sheng, Y. Zhang, M. Zhang, P. Qu, S. Wang, *J. Mater. Res. Technol.* **2023**, 26, 5488.
- [23] S. Guo, X. Sheng, A. Guo, W. Yang, X. Zhao, S. Sui, J. Li, Y. Zhao, M. Wang, X. Lin, *J. Mater. Res. Technol.* **2025**, 35, 2158.
- [24] W. Schneller, M. Leitner, S. Pomberger, F. Grün, S. Leuders, T. Pfeifer, O. Jantschner, *Addit. Manuf.* **2021**, 40, 101930.
- [25] E. Beevers, A. D. Brandão, J. Gumpinger, M. Gschweilt, C. Seyfert, P. Hofbauer, T. Rohr, T. Ghidini, *Int. J. Fatigue* **2018**, 117, 148.
- [26] J. N. Domfong Ngnekou, Y. Nadot, G. Henaff, J. Nicolai, L. Ridosz, *Procedia Struct. Integr.* **2017**, 7, 75.
- [27] M. Braun, E. Mayer, I. Kryukov, C. Wolf, S. Böhm, A. Taghipour, R. E. Wu, S. Ehlers, S. Sheikhi, *Fatigue Fract. Eng. Mater. Struct.* **2021**, 44, 3077.
- [28] S. P. Narra, A. D. Rollett, A. Ngo, D. Scannapieco, M. Shahabi, T. Reddy, J. Pauza, H. Taylor, C. Gobert, E. Diewald, F. X. Dugast, A. To, R. Wicker, J. Beuth, J. J. Lewandowski, *J. Mater. Process. Technol.* **2023**, 311, 117775.
- [29] N. Soro, N. Saintier, J. Merzeau, M. Veidt, M. S. Dargusch, *Addit. Manuf.* **2021**, 37, 101653.
- [30] H. Neuber, *Theory of Notch Stresses: Principles for Exact Stress Calculation*, J.W. Edwards Publishing **1945**.
- [31] B. Van Hooreweder, J.-P. Kruth, *CIRP Ann.* **2017**, 66, 221.

- [32] M.-W. Wu, J.-K. Chen, B.-H. Lin, P.-H. Chiang, *Mater. Des.* **2017**, 134, 163.
- [33] A. Zargarian, M. Esfahanian, J. Kadkhodapour, S. Ziaei-Rad, D. Zamani, *Theor. Appl. Fract. Mech.* **2019**, 100, 225.
- [34] F. Collini, G. Meneghetti, *Mater. Des.* **2024**, 244, 113077.
- [35] A. Coluccia, G. De Pasquale, *Sci. Rep.* **2023**, 13, 22775.
- [36] A. Burr, T. Persenot, P.-T. Dautre, J.-Y. Buffiere, P. Lhuissier, G. Martin, R. Dendievel, *Int. J. Fatigue* **2020**, 139, 105769.
- [37] S. A. Khairallah, A. T. Anderson, A. Rubenchik, W. E. King, *Acta Mater.* **2016**, 108, 36.
- [38] P. P. Milella, *Fatigue and Corrosion in Metals*, Springer Milan, Milano **2013**.
- [39] L. S. Kollmannsperger, O. Maurer, R. Kose, A. T. Zeuner, D. Bähre, S. C. L. Fischer, *Commun. Eng.* **2024**, 3, 56.
- [40] C. Pan, Y. Han, J. Lu, *Appl. Sci.* **2020**, 10, 6374.
- [41] Nikon SLM Solutions **2019**.
- [42] M. Möser, *Engineering Acoustics: An Introduction to Noise Control*, Springer Berlin Heidelberg, Berlin, Heidelberg **2009**.
- [43] A. D. Pierce, *Acoustics: An Introduction To Its Physical Principles and Applications*, Springer International Publishing, Cham **2019**.
- [44] O. Maurer, H. Jacob, D. Bähre, *Powders* **2024**, 3, 154.
- [45] B. Beausir, J.-J. Fundenberger **2017**.
- [46] R. Acharya, J. A. Sharon, A. Staroselsky, *Acta Mater.* **2017**, 124, 360.
- [47] E. Brandl, U. Heckenberger, V. Holzinger, D. Buchbinder, *Mater. Des.* **2012**, 34, 159.
- [48] M. J. Paul, Q. Liu, J. P. Best, X. Li, J. J. Kruzic, U. Ramamurty, B. Gludovatz, *Acta Mater.* **2021**, 211, 116869.
- [49] E. Sert, E. Schuch, A. Öchsner, L. Hitzler, E. Werner, M. Merkel, *Materialwiss. Werkstofftech.* **2019**, 50, 539.
- [50] Mathworks Inc. **2022**.